Photon transport in cylindrically-shaped disordered meso-macroporous materials

P. Gaikwad, S. Ungureanu, R. Backov, Kevin Vynck, Renaud A. L. Vallée

P. Gaikwad, S. Ungureanu, R. Backov, Kevin Vynck, Renaud A. L. Vallée. Photon transport in cylindrically-shaped disordered meso-macroporous materials. Optics Express, 2014, 22 (7), pp.7503-7513. 10.1364/OE.22.007503 . hal-00965290

Photon transport in cylindrically-shaped disordered meso-macroporous materials

P. Gaikwad,[1] **S. Ungureanu,**[1] **R. Backov,**[1] **K. Vynck,** [2,3] **and R. A. L. Vallée** [1,*]

[1] *CNRS, University Bordeaux, CRPP, UPR 8641, 115 av. Schweitzer, 33600 Pessac, France*
[2] *Laboratoire Photonique, Numérique et Nanosciences (LP2N), UMR 5298, CNRS - IOGS - Univ. Bordeaux, Institut d'Optique d'Aquitaine, 33400 Talence, France*
[3]*kevin.vynck@institutoptique.fr*
[*]*vallee@crpp-bordeaux.cnrs.fr*

Abstract: We theoretically and experimentally investigate light diffusion in disordered meso-macroporous materials with a cylindrical shape. High Internal Phase Emulsion (HIPE)-based silica foam samples, exhibiting a polydisperse pore-size distribution centered around 19 μm to resemble certain biological tissues, are realized. To quantify the effect of a finite lateral size on measurable quantities, an analytical model for diffusion in finite cylinders is developed and validated by Monte Carlo random walk simulations. Steady-state and time-resolved transmission experiments are performed and the transport parameters (transport mean free path and material absorption length) are successfully retrieved from fits of the experimental curves with the proposed model. This study reveals that scattering losses on the lateral sides of the samples are responsible for a lowering of the transmission signal and a shortening of the photon lifetime, similar in experimental observables to the effect of material absorption. The recognition of this geometrical effect is essential since its wrong attribution to material absorption could be detrimental in various applications, such as biological tissue diagnosis or conversion efficiency in dye-sensitized solar cells.

OCIS codes: (290.4210) Multiple scattering; (290.5820) Scattering measurements; (290.5825) Scattering theory.

References and links

1. A. B. Davis and A. Marshak, "Solar radiation transport in the cloudy atmosphere: a 3D perspective on observations and climate impacts," Rep. Prog. Phys. **73**, 026801 (2010).
2. S. Chandrasekhar, *Radiative Transfer* (Dover Publications, 2011).
3. G. Reich, "Near-infrared spectroscopy and imaging: Basic principles and pharmaceutical applications," Adv. Drug Delivery Rev. **57**, 1109 (2005).
4. H. W. Siesler, Y. Ozaki, S. Kawata, and H. M. Heise, "Near-Infrared Spectroscopy: Principles, Instruments, Applications" (Wiley, New York, 2008).
5. V. V. Tuchin, *Tissue Optics: Light Scattering Methods and Instruments for Medical Diagnosis*, 2nd ed. (SPIE, Bellingham, WA, 2007).
6. L. V. Wang and H.-i. Wu, *Biomedical Optics: Principles and Imaging* (Wiley, New York, 2007).
7. M. S. Patterson, B. Chance, and B. C. Wilson, "Time resolved reflectance and transmittance for the noninvasive measurement of tissue optical properties," Appl. Opt. **28**, 2331–2336 (1989).
8. D. A. Benaron, and D. K. Stevenson, "Optical time-of-flight and absorbance imaging of biologic media," Science **259**, 1463–1466 (1993).

#206709 - $15.00 USD
Received 18 Feb 2014; accepted 7 Mar 2014; published 24 Mar 2014

9. T. Svensson, E. Alerstam, D. Khoptyar, J. Johansson, S. Folestad, and S. Andersson-Engels, “Near-infrared photon time-of-flight spectroscopy of turbid materials up to 1400 nm,” Rev. Sci. Instrum. **80**, 063105 (2009).
10. V. Backman, M. B. Wallace, L. T. Perelman, J. T. Arendt, R. Gurjar, M. G. Müller, Q. Zhang, G. Zonios, E. Kline, T. McGillican, S. Shapshay, T. Valdez, K. Badizadegan, J. M. Crawford, M. Fitzmaurice, S. Kabani, H. S. Levin, M. Seiler, R. R. Dasari, I. Itzkan, J. Van Dam, and M. S. Feld, “Detection of preinvasive cancer cells,” Nature **406**, 35–36 (2000).
11. E. Alerstam and T. Svensson, “Observation of anisotropic diffusion of light in compacted granular porous materials,” Phys. Rev. E **89**, 040301(R) (2012).
12. T. Svensson, M. Andersson, L. Rippe, S. Svanberg, S. Andersson-Engels, J. Johansson and S. Folestad, “VCSEL-based oxygen spectroscopy for structural analysis of pharmaceutical solids,” Appl. Phys. B **90**, 345–354 (2008).
13. Z. Shi, and C. A. Anderson, “Pharmaceutical applications of separation of absorption and scattering in near-infrared spectroscopy (NIRS),” J. Pharm. Sci. **99**, 4766–4783 (2010).
14. C. M. Leroy, C. Olivier, T. Toupance, M. Abbas, L. Hirsch, S. Ravaine and R. Backov, “One-pot easily-processed TiO_2 macroporous photoanodes (Ti-HIPE) for dye-sensitized solar cells,” Sol. State Sci. **28**, 81–89 (2014).
15. A. Ishimaru, *Wave Propagation and Scattering in Random Media* (Wiley-IEEE Press, 1999).
16. D. Contini, F. Martelli, and G. Zaccanti, “Photon migration through a turbid slab described by a model based on diffusion approximation. I. Theory,” Appl. Opt. **36**, 4587–4599 (1997).
17. M. C. W. van Rossum, and Th. M. Nieuwenhuizen, “Multiple scattering of classical waves: microscopy, mesoscopy, and diffusion,” Rev. Mod. Phys. **71**, 313–371 (1999).
18. E. Akkermans, and G. Montambaux, *Mesoscopic Physics of Electrons and Photons* (Cambridge University Press, 2007).
19. A. Z. Genack, J. M. Drake, “Relationship between Optical Intensity, Fluctuations and Pulse Propagation in Random Media,” Europhys. Lett. **11**, 4331–4336 (1990).
20. P. D. Garcia, R. Sapienza, J. Bertolotti, M. D. Martín, Á. Blanco, A. Altube, L. Vina, D. S. Wiersma, and C. López, “Resonant light transport through Mie modes in photonic glasses,” Phys. Rev. A **78**, 023823 (2008).
21. T. van der Beek, P. Barthelemy, P. M. Johnson, D. S. Wiersma, and A. Lagendijk, “Light transport through disordered layers of dense gallium arsenide submicron particles,” Phys. Rev. B **85**, 115401 (2012).
22. M. Vellekoop, A. P. Mosk, “Focusing coherent light through opaque strongly scattering media,” Opt. Lett. **32**, 2309–2311 (2007).
23. S. M. Popoff, G. Lerosey, R. Carminati, M. Fink, A. C. Boccara, and S. Gigan, “Measuring the Transmission Matrix in Optics: An Approach to the Study and Control of Light Propagation in Disordered Media,” Phys. Rev. Lett. **104**, 100601 (2010).
24. R. Savo, M. Burresi, T. Svensson, K. Vynck, and D. S. Wiersma, “Measuring the fractal dimension of an optical random walk,” arXiv:1312.5962.
25. N. Ghofraniha, I. Viola, A. Zacheo, V. Arima, G. Gigli, and C. Conti, “Transition from nonresonant to resonant random lasers by the geometrical confinement of disorder,” Opt. Lett. **38**, 5043–5046 (2013).
26. F. Carn, A. Colin, M-.F. Achard, M. Pirot, H. Deleuze and R. Backov, “Inorganic monoliths hierarchically textured via concentrated direct emulsion and micellar templates,” J. Mat. Chem. **14**, 1370–1376 (2004).
27. D. Barby and Z. Haq, “Low density porous cross-linked polymeric materials and their preparation,” Eur. Patent Appl. 60138 (1982).
28. M. J. Mooney, “The viscosity of a concentrated suspension of spherical particles,” J. Colloid. Interface Sci. **6**, 162–170 (1951).
29. T. G. Mason, J. Bibette, and D. A. Weitz, “Yielding and Flow of Monodisperse Emulsions,” J. Colloid. Interface Sci. **179**, 439–448 (1996).
30. M.-P. Aronson and M.-F. Petko, “Highly Concentrated Water-in-Oil Emulsions: Influence of Electrolyte on Their Properties and Stability,” J. Colloid Interface Sci. **159**, 134–149 (1993).
31. C. J. Brinker and G. W. Scherer, in *Sol-Gel Science: the Physics and Chemistry of Sol-Gel Processing* (Academic Press, San Diego, 1990).
32. J. X. Zhu, D. J. Pine, and D. A. Weitz, “Internal reflection of diffusive light in random media,” Phys. Rev. A **44**, 3948–3959 (1991).
33. L.-H. Wang, S. L. Jacques, and L.-Q. Zheng, ”Monte Carlo modeling of photon transport in multi-layered tissues,” Computer Methods and Programs in Biomedicine **47**, 131–146 (1995).
34. M. Xu and R. R. Alfano, “Random walk of polarized light in turbid media,” Phys. Rev. Lett. **95**, 213901 (2005).
35. R. Elaloufi, R. Carminati, and J.-J. Greffet, “Diffusive-to-ballistic transition in dynamic light transmission through thin scattering slabs: a radiative transfer approach,” J. Opt. Soc. Am. A **21**, 1430–1437 (2004).
36. A. Sihvola, *Electromagnetic Mixing Formulae and Applications* (The Institution of Engineering and Technology, 1999).
37. A. S. Gittings, R. Bandyopadhyay, and D. J. Durian, “Photon channelling in foams,” Europhys. Lett. **65**, 414–419 (2004).
38. M. Schmiedeberg , M. F. Miri, and H. Stark, “Photon channelling in foams,” Eur. Phys. J. E **18**, 123–131 (2005).
39. T. Svensson, K. Vynck, M. Grisi, R. Savo, M. Burresi, and D. S. Wiersma, “Holey random walks: Optics of heterogeneous turbid composites,” Phys. Rev. E **87**, 022120 (2013).

Received 18 Feb 2014; accepted 7 Mar 2014; published 24 Mar 2014

1. Introduction

Disordered optical media are ubiquitous in nature, and a proper description of light propagation in such materials is crucial for a number of applications, ranging from the study of radiation transport in the atmosphere [1, 2] to the optical characterization of complex materials [3, 4], to the optical diagnosis of the human body [5, 6]. In biomedical and material sciences, optical (or photon) time-of-flight spectroscopy has been used quite extensively to infer the microscopic properties of turbid media (density and size of the scattering heterogeneities, intrinsic absorption, ...) from macroscopic observables (typically, the time-resolved transmission) [7–9]. Light scattering is in general a valuable tool for the detection of compositional or structural changes in complex media, e.g. epithelial tissues for early cancer detection [10] and compacted granular materials [11]. Recent developments in the field have important implications for quantitative spectroscopy of porous materials, such as pharmaceutical tablets [12, 13] or even macroporous photoanodes in dye-sensitized solar cells [14].

When light experiences many scattering events in a disordered material and the scattering mean free path is much larger than the wavelength, macroscopic transport can be well described by a classical diffusion equation [15]. For practical convenience in theory and experiments, it is then common to consider disordered media in slab geometries, where the sample is finite along one direction and assumed infinite along the other two directions. Analytical expressions for the steady-state and time-resolved optical responses in slabs are well-established [7, 16–18] and such geometries are commonly used in studies on wave phenomena in disordered media [19–24]. However, in several situations, such as samples of biological tissues or of pharmaceutical solids, as discussed above, the systems can differ from an ideal slab geometry. The macroscopic dimensions of the sample and the related boundary conditions are expected to affect the overall diffusion process and the resulting optical phenomenon under study (see, e.g., [25] on random lasing). Properly assessing the microscopic properties of disordered media therefore requires taking these characteristics into account.

In this paper, we investigate light diffusion in cylindrically-shaped disordered materials, where the samples diameter is comparable to their thickness. Our scope is to describe quantitatively the effect of the finite lateral sample size on measurable quantities. For this purpose, we merge together knowledge in multiple light scattering and in material design and fabrication. The samples are High Internal Phase Emulsion (HIPE)-based silica foams, engineered such that they exhibit a polydisperse pore-size distribution similar to certain biological tissues. Fabrication and structural characterization details are given in Sec. 2. In Sec. 3, we present a diffusion model to obtain analytical expressions for the steady-state and time-resolved transmission along the cylinder axis, and validate it with Monte Carlo simulations of random walks in finite cylinders. The steady-state and time-resolved optical experiments, performed on samples of different thicknesses, are presented in Sec. 4. An important finding is that lateral scattering losses can easily be misinterpreted as material absorption, which would clearly be detrimental to the optical spectroscopy of turbid media in general (biological tissues, colloids, powders, etc). Nevertheless, we show that the correct transport parameters (transport mean free path and material absorption length) can be retrieved with good accuracy from fits of the experimental curves with the derived analytical expressions.

2. Material fabrication and structural characterization

A state-of-the-art bottom-up approach was used to realize strongly scattering HIPE-based silica foam samples with well-controlled morphologies and textures (wall thickness, curvatures, textural topologies, degree of mesoporosity and cell diameter) [26]. This emulsion route to prepare porous hierarchical structures allows light to penetrate the porous matrices through the internal surface specificity. The density and size distribution of the pores (which determine the disor-

#206709 - $15.00 USD Received 18 Feb 2014; accepted 7 Mar 2014; published 24 Mar 2014

dered state of the foams) can be controlled through the adjustment of the oil volumic fraction f and the shearing rate.

Tetraetoxy-orthosilane ($Si(OEt)_4$, TEOS) and tetradecyltrimethylammonium bromide 98% (C_{14} H_{29} $NBr(CH_3)$, TTAB) were purchased from Fluka, HCl 37% and dodecane 99% were purchased from Prolabo. Procedures are based on the use of both micelles and direct concentrated emulsion templates [26]. Typically 5.7 g of TEOS are added to 16.5 g of TTAB aqueous solution at 35% in weight. The aqueous mixture is then brought to a pH value close to 0 (6.7 mL of HCl 37%) leading, after the oil emulsification process, to the materials labelled as SiO_2(HIPE). These macrocellular foams emerge from the use of a starting concentrated direct emulsion at oil volumic fraction ($f = 0.67$), where 35 g of dodecane are emulsified.

SEM observations were performed with a Jeol JSM-840A scanning electron microscope operating at 10 kV. The specimens were gold-coated or carbon-coated prior to examination. Final inorganic monolith-type materials (Fig. 1(a) and inset) depict typical polymerized HIPE-type interconnected macroporous textures with polydisperse cellular sizes within the micrometer range [27]. At this point we would like to note that we call windows the holes that separate two adjacent macroscopic cells. For the starting emulsion oil volumic fraction $f = 0.67$, the macrocellular cell sizes are in the range 5-50 μm, with a mean value of 19 μm and a standard deviation of 9.6 μm (Fig. 1(b)). Such a foam closely resembles a population of epithelial cells [10], as mentioned previously, and could therefore have an interest for biological tissue diagnosis.

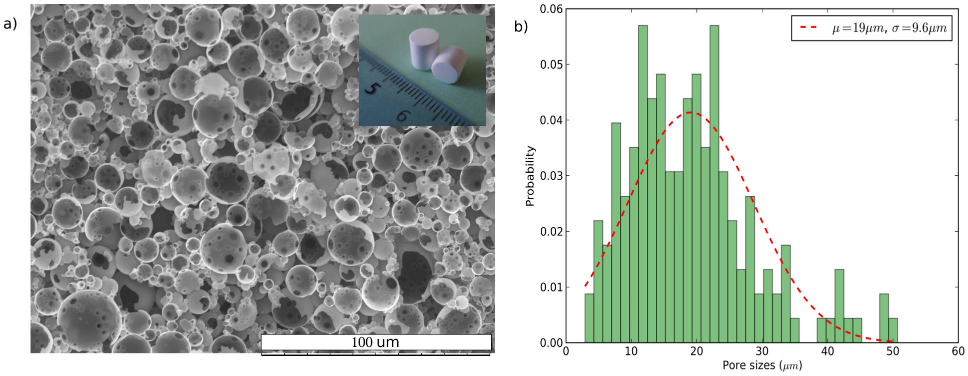

Fig. 1. (a) SEM micrograph of the SiO_2(HIPE) and (b) normalized distribution (green histogram) of pore diameters. The normal probability distribution function determined from the arithmetic mean and standard deviation of the pore sizes is also shown (red dashed line). The inset of (a) shows 2 monoliths of different thicknesses, evidencing the equivalence of the lateral and longitudinal dimensions.

Considering the emulsion rheology, it is well known that the viscosity of direct emulsions increases dramatically when the oil volumic fraction are reaching values above $f = 0.74$ [28–30]. This phenomenon increases the stress applied on the oily droplets, inducing smaller macrocellular cells within the solid stat replica. For the starting emulsions of the SiO_2(HIPE) materials considered here, we do not reach this limit. The macroporous monolithic texture resembles aggregated polydisperse hollow spheres. In such low pH conditions, the polycondensation is strongly Euclidian [31] (dense) and starts at the oil/water interface. The latter is promoting silica condensation by minimizing the nucleation enthalpy, acting so as a defect [27]. As the oil-water interface of an emulsion is associated to a higher surfactant concentration than the

#206709 - $15.00 USD Received 18 Feb 2014; accepted 7 Mar 2014; published 24 Mar 2014

core of the continuous aqueous phase [28–30], this specific region of high surfactant concentration is also enhancing silica condensation by minimizing electrostatic repulsions.

In order to both provide foams skeletal, bulk densities and quantify the macroscale void windows distributions, we performed mercury intrusion porosimetry measurements (Table 2). It is worth mentioning that this technique measures the size of the macroscopic pore "windows" between the emulsion templated cells and not the diameter of the cells themselves. The skeleton density is below 1.2 (silica density) because the foam walls are indeed bearing a large degree of mesoporosity with polydisperse (vermicular type) pore sizes ranging from 1 to 2 nm [26].

Table 1. Oil volumic fraction of the starting emulsion and Mercury intrusion porosimetry results.

Material	Oil volumic fraction	Intrusion volume (cm^3/g)	Porosity (%)	Skeleton density (g/cm^3)	Bulk density (g/cm^3)
$SiO_2(HIPE)$	0.67	10	91	1	0.083

For the optical experiments in this study, we manufactured 25 samples with thicknesses varying between about 1 and 10 mm and a fixed radius of 3.5 mm (Fig. 1(a), inset). The monoliths therefore have a lateral size comparable to their thickness, requiring the development of a theoretical model for diffusion in finite cylinders.

3. Theory and simulations

3.1. Model of diffusion in finite cylinders

We start from the diffusion equation for the energy density $u(\mathbf{r},t)$

$$D\nabla^2 u(\mathbf{r},t) = \frac{\partial u(\mathbf{r},t)}{\partial t} + \mu_a v u(\mathbf{r},t), \tag{1}$$

where $D = v\ell_t/3$ is the diffusion constant for a statistically homogeneous and isotropic disordered medium, v is the energy velocity in the medium, ℓ_t is the transport mean free path and $\mu_a = 1/\ell_a$ is the absorption coefficient of the material (ℓ_a being the material absorption length). Considering invariance by rotation around the cylinder axis (say along z), the Laplacian operator can be written in cylindrical coordinates as

$$\nabla^2 u(\rho,z,t) = \frac{1}{\rho}\frac{\partial u(\rho,z,t)}{\partial \rho} + \frac{\partial^2 u(\rho,z,t)}{\partial \rho^2} + \frac{\partial u(\rho,z,t)}{\partial z}. \tag{2}$$

Performing the standard approach of separation of variables $u(\rho,z,t) = P(\rho)Z(z)T(t)$, the diffusion equation leads to a system of three differential equations which can be solved directly to give

$$T(t) = \exp\left[-(\lambda_\rho + \lambda_z + \mu_a v)t\right], \tag{3}$$

$$Z(z) = C_1 \cos\left[\sqrt{\frac{\lambda_z}{D}} z\right] + C_2 \sin\left[\sqrt{\frac{\lambda_z}{D}} z\right], \tag{4}$$

$$P(\rho) = C_3 J_0\left[\sqrt{\frac{\lambda_\rho}{D}} z\right] + C_4 Y_0\left[\sqrt{\frac{\lambda_\rho}{D}} z\right]. \tag{5}$$

Here, C_1, C_2, C_3 and C_4 are constants, J_0 and Y_0 are zeroth-order Bessel functions of the first and second kinds, respectively, and λ_z and λ_ρ are the eigenvalues of the differential operators in z and ρ, respectively.

Received 18 Feb 2014; accepted 7 Mar 2014; published 24 Mar 2014

The constants and the eigenvalues are determined by applying the boundary conditions to $u(\rho,z,t)$. The physical dimensions of the cylindrical system are defined by its radius R and its length L, see Fig. 2(a). Due to the outgoing flux, the energy density in the medium does not equal zero at the physical boundaries but at a distance $l_e = \frac{1+r}{1-r}\frac{2}{3}\ell_t$ away from it, where r is the internal reflection coefficient and ℓ_t the transport mean free path [32]. We therefore apply absorbing boundary conditions on a system with extrapolated radius $R_e = R + l_e$ and length $L_e = L + 2l_e$. The boundary conditions are the following.

$$u(\rho, z = 0, t) = 0, \tag{6}$$

$$u(\rho, z = L_e, t) = 0, \tag{7}$$

$$u(\rho = 0, z, t) \neq \pm\infty, \tag{8}$$

$$u(\rho = R_e, z, t) = 0. \tag{9}$$

From these conditions, we find a discrete set of eigenvalues, $\lambda_{\rho,m} = (\alpha_m/R_e)^2 D$ and $\lambda_{z,n} = (n\pi/L_e)^2 D$, where α_m is the mth zero of J_0. By applying the orthogonality relation between eigenmodes over the extrapolated volume of the system, we obtain an expression for the energy density:

$$\begin{aligned} u(\rho,z,t) \quad = \quad & \frac{2}{\pi L_e R_e^2} \sum_{m=1}^{\infty} \frac{1}{J_1^2(\alpha_m)} J_0\left[\frac{\alpha_m}{R_e}\rho\right] \exp\left[-\frac{\alpha_m^2}{R_e^2}Dt\right] \\ & \times \sum_{n=1}^{\infty} \sin\left[\frac{n\pi}{L_e}z_0\right] \sin\left[\frac{n\pi}{L_e}z\right] \exp\left[-\frac{n^2\pi^2}{L_e^2}Dt\right] \exp\left[-\mu_a v t\right]. \end{aligned} \tag{10}$$

In this last step, we assumed the initial energy density distribution (at $t = 0$) to be a disk of radius l_ε at a depth $z = z_0$, i.e. $u(\rho,z,0) = \delta(z - z_0)\Theta(l_\varepsilon - r)\frac{1}{\pi l_\varepsilon^2}$, where Θ is the Heaviside function, and took the limit $l_\varepsilon \to 0$ to have a point source.

The energy flux is calculated using first Fick's law of diffusion

$$\mathbf{J} = -D\nabla u(\rho,z,t) = -D\left[\frac{\partial u(\rho,z,t)}{\partial \rho}\hat{\rho} + \frac{\partial u(\rho,z,t)}{\partial z}\hat{z}\right]. \tag{11}$$

In practice, we are only interested in the flux that is transmitted (or reflected) along the z-axis, such that we can limit ourselves to the calculation of $J_z = -D\frac{\partial u(\rho,z,t)}{\partial z}$. The partial derivative of $u(\rho,z,t)$ with z is straightforward and leads to

$$\begin{aligned} J_z(\rho,z,t) \quad = \quad & -\frac{2D}{L_e^2 R_e^2} \sum_{m=1}^{\infty} \frac{1}{J_1^2(\alpha_m)} J_0\left[\frac{\alpha_m}{R_e}\rho\right] \exp\left[-\frac{\alpha_m^2}{R_e^2}Dt\right] \\ & \times \sum_{n=1}^{\infty} n \sin\left[\frac{n\pi}{L_e}z_0\right] \cos\left[\frac{n\pi}{L_e}z\right] \exp\left[-\frac{n^2\pi^2}{L_e^2}Dt\right] \exp\left[-\mu_a v t\right]. \end{aligned} \tag{12}$$

To have the time-resolved transmission through a plane normal to the z-axis, we should integrate J_z over the surface, as $T(z,t) = 2\pi\int_0^R J_z(\rho,z,t)\rho d\rho$, yielding

$$\begin{aligned} T(z,t) \quad = \quad & -\frac{4\pi D R}{L_e^2 R_e} \sum_{m=1}^{\infty} \frac{1}{\alpha_m J_1^2(\alpha_m)} J_1\left[\frac{\alpha_m}{R_e}R\right] \exp\left[-\frac{\alpha_m^2}{R_e^2}Dt\right] \\ & \times \sum_{n=1}^{\infty} n \sin\left[\frac{n\pi}{L_e}z_0\right] \cos\left[\frac{n\pi}{L_e}z\right] \exp\left[-\frac{n^2\pi^2}{L_e^2}Dt\right] \exp\left[-\mu_a v t\right]. \end{aligned} \tag{13}$$

Received 18 Feb 2014; accepted 7 Mar 2014; published 24 Mar 2014

Finally, to get the total (steady-state) transmission (or reflection) along the z-axis of the cylinder, it is sufficient to integrate $T(z,t)$ over time as $T(z) = \int_0^\infty T(z,t)dt$, leading to

$$T(z) = -\frac{4\pi R}{L_e^2 R_e} \sum_{m=1}^{\infty} \sum_{n=1}^{\infty} \frac{J_1\left[\frac{\alpha_m}{R_e} R\right] n \sin\left[\frac{n\pi}{L_e} z_0\right] \cos\left[\frac{n\pi}{L_e} z\right]}{\alpha_m J_1^2(\alpha_m) \left(\frac{\alpha_m^2}{R_e^2} + \frac{n^2\pi^2}{L_e^2} + \frac{\mu_a v}{D}\right)}. \qquad (14)$$

One can verify that, when $R \to \infty$, Eqs. (13) and (14) converge correctly to the solutions for slab geometries. Equations (13) and (14) hold for all values of R and L and therefore generalize the standard expressions for slab geometries.

3.2. *Comparison with Monte Carlo simulations*

We now compare the analytical expressions for the time-resolved and steady-state transmission, Eqs. (13) and (14), with Monte Carlo simulations of unpolarized random walks in 3D finite cylinders, described schematically in Fig. 2(a) [33]. After many scattering events, the light polarization is completely scrambled, such that it can be safely omitted in the transport of the average energy density [34]. For the sake of simplicity, we consider a non-absorbing ($\mu_a = 0$) medium with a refractive index of 1 such that internal reflections can be neglected ($r = 0$) and $v = 300$ μm/ps. We recall that $R_e = R + l_e$, $L_e = L + 2l_e$ and $l_e = \frac{2}{3}\ell_t$. The source should be placed one transport mean free path away from the physical boundary, i.e. $z_0 = l_e + \ell_t$, and the transmitted flux should be calculated at the physical boundary, i.e. $z = l_e + L$.

Diffusion theory works well when the dimensions of the system, R and L, are both much larger than the transport mean free path ℓ_t (typically by a factor of about 10) [35]. In addition, since we seek for situations in which the standard model of diffusion in slabs is inadequate, the sample diameter should be comparable to its thickness. To validate our model, we therefore choose the following parameters: $\ell_t = 5$ μm and $L = R = 100$ μm. The statistics was made on a total of 10^7 random walkers (10 realizations of 10^6 random walkers).

The results for the time-resolved transmission are shown in Fig. 2(b), where an excellent agreement is found between the Monte Carlo simulations and our theoretical prediction for a finite cylinder, Eq. (13), while a strong deviation with the theoretical prediction for a slab is observed (see analytical expression in, e.g., [16]). The exponential decay rate in a slab configuration, $\Gamma = 0.4337$ ps^{-1}, is underestimated by about 38 % ($\Gamma = 0.7045$ ps^{-1}). An excellent agreement is also observed on the total transmission through the cylinder, where Monte Carlo simulations yield $T = 0.049777 \pm 0.000431$ (95 % confidence interval) and Eq. (14) $T = 0.049483$, while the theoretical prediction for a slab gives $T = 0.078125$, that is overestimated by about 58 %. On this last point, we should point out that a very large number of terms in the sum over the sines and cosines is in general necessary to achieve convergence (here, $max[n] = 20000$), while much fewer are needed for the Bessel functions (here, $max[m] = 10$). In sum, this comparison with numerical calculations validates our theoretical model and proves very clearly the inadequacy of the diffusion model for slabs in such systems. Clearly, the deviation of the results between slab and cylinder configurations should diminish with increasing ratio R/L.

4. Experiments and discussion

Let us first recall the structural and material parameters of the samples. The sample thickness L was varied between about 1 and 10 mm and their radius R was fixed to 3.5 mm. According to the mercury intrusion porosimetry measurements (Table 2), the samples are composed by 91 % of air (in the form of inclusions) and, thus, 9 % of mesoporous SiO_2 with permittivity around 2.1. From these considerations and using the Maxwell Garnett mixing rule [36], we find

Received 18 Feb 2014; accepted 7 Mar 2014; published 24 Mar 2014

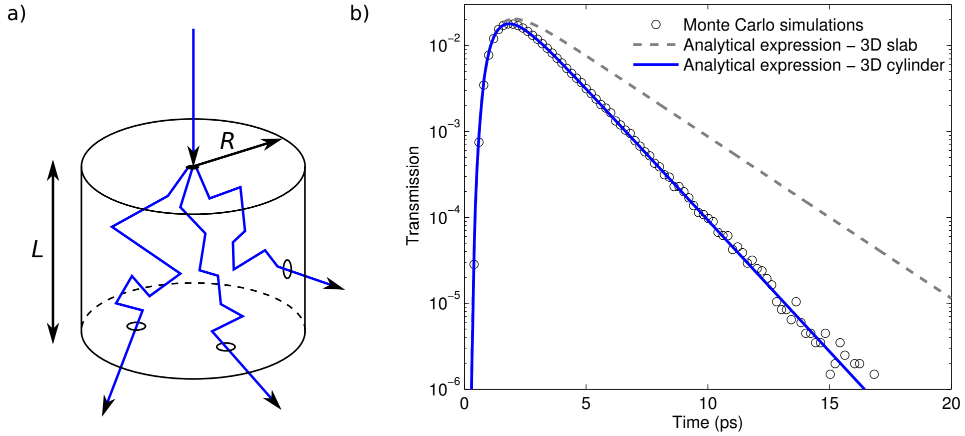

Fig. 2. (a) Sketch of the Monte Carlo simulations. Random walkers are launched on a side of the cylinder (here, top side). Those that cross the other (bottom) side are counted in the transmission measurements. (b) Time-resolved transmission curves through a cylinder with thickness $L = 100\ \mu$m, radius $R = 100\ \mu$m and transport mean free path $\ell_t = 5\ \mu$m, obtained from Monte Carlo simulations (hollow dots), the analytical expression derived for slabs [16] (gray dashed line), and the analytical expression in Eq. (13) derived for finite cylinders (blue solid line). The agreement between the Monte Carlo simulations and the model for diffusion in finite cylinders is excellent, while a clear deviation is observed with the model for diffusion in slabs. The faster decay observed in the case of the cylinder could be wrongly interpreted as material absorption.

that the effective refractive index of the medium for light propagation is $n_{eff} \approx 1.04$. This is expected to modify slightly the average energy velocity in the medium $v = c/n_{eff}$, which enters the diffusion constant expression D, and yield a weak internal reflection coefficient $r \approx 0.059$ in the expression of the extrapolated length l_e [32]. At this point, two important comments are in place. First, one should realize that light propagation in foams with macroscopic inclusions differs quite significantly from that in more common powder-like samples, since light tends to propagate via the inclusion walls [37,38]. The behavior of light at a sample interface may actually not be captured by an effective medium approach. In our samples, however, the dielectric contrast is very weak such that it is not expected to yield important changes in the diffusion properties reported below. Second, one should be aware that the common expression of the diffusion constant, $D = v\ell_t/3$, applies exclusively to disordered media exhibiting a statistically homogeneous distribution of scatterers. A more general formula for D was derived recently for media containing arbitrary pore-size distributions [39]. Considering the fair polydispersity of our samples, we expect the deviation on the retrieved ℓ_t to be smaller than the accuracy of our measurements. Nevertheless, we believe that this could be an interesting aspect to consider in future investigations.

The total (steady-state) transmittance was determined on the whole visible spectrum from measurements of the total integrated forward scattering through the surface owing to a white light illumination lamp (fiber coupled white light HL-2000-HP-FHSA, Ocean Optics) combined with an integrating sphere (fiber coupled integrating sphere FOIS-1, Ocean Optics) and a spectrometer (fiber spectrometer USB2000+VIS-NIR, Ocean Optics). The time-resolved transmission profiles were obtained from a histogram of time delays for single photons travelling across the sample relative to the incident pulse, and were recorded with a time-resolved setup consisting of a streak camera (HAMAMATSU Streak Scope C10627). The excitation light was the frequency doubled output of the $\lambda = 1030$ nm wavelength, 10 MHz repetition rate, 300 fs line width pulses delivered by a diode-pumped Ytterbium femtosecond oscillator from Amplitude systems (t-Pulse 200). The beam was focussed to a 1 mW, 100 μm spot diameter on the slab; the transmission intensity was focussed on the entrance slit of the spectrograph.

Results for the steady-state transmission are shown in Fig. 3(a) for the 25 considered samples. Obviously, for each wavelength, the transmittance is a decreasing function of the sample thickness. Figure 3(b) shows the transmittance at a wavelength of 515 nm (for which subsequent time-resolved measurements will be performed) as a function of sample thickness. Clearly, it does not follow the well-known Ohm's law, which predicts that $T \propto \frac{\ell_t}{L}$ [18]. Instead of a straight line with a -1 slope on the log-log plot (black solid line), a more complex behavior is found, with a linear trend only present up to thicknesses of about 2 mm. A fit of these data with the stationary solution of the standard diffusion equation including absorption [20] yields $\ell_t = 53 \pm 18$ μm and $\ell_a = 1/\mu_a = 1.57 \pm 0.21$ mm (black dashed line), which is of the order of the samples size. Although the fit appears to be good, we remark that the deviation from the linear trend occurs when the thickness of the cylinder becomes comparable to its radius, a situation in which the lateral size of the sample simply cannot be neglected. This absorption length thus appears to account, at least partly, for the lateral "scattering losses". This is verified by fitting the experimental data with the analytical expression for the total transmission through finite diffusive cylinders, Eq. (14), yielding $\ell_t = 48 \pm 0.4$ μm and $\ell_a = 0.95 \pm 0.35$ m (red dashed line). This very long absorption length demonstrates that indeed the large decrease of the transmittance curve with sample thickness is a result of the finite lateral size of the SiO_2(HIPE) monoliths and not to the material absorption. The curve expected for $\ell_t = 48$ μm and no absorption is also shown for comparison (red solid line), confirming that the actual role of material absorption is minor.

Besides these steady-state transmission measurements, performed as a function of sample thickness, it is interesting to validate the retrieved values on single samples. Most applications of the technique would indeed be performed with the use of only one specimen. Time-dependent scattering allows to determine both ℓ_t and ℓ_a with a single measurement [19, 20]. Fig. 3(c) shows the time-of-flight experiments performed on two SiO_2(HIPE) samples with thicknesses 3.2 mm (red stars) and 6.9 mm (blue circles). These profiles correspond to the convoluted responses of the instrument and of the monolith. Clearly, the samples exhibit a strongly multi-diffusive character, with photons being significantly delayed in the sample in both cases. As the thickness of the sample increases, so does the mean exit time of light. A small crack in the 6.9-mm thick sample (blue circles) caused a part of the excitation pulse to exit early, as observed by the shoulder at about 0.4 ns. These experimental temporal profiles have been compared to the predictions of the diffusion model in finite cylinders, Eq. (13), with the parameters determined previously, i.e. $\ell_t = 48$ μm and $\ell_a = 0.95$ m. Fig. 3(c) shows the predicted curves (solid lines), which are the convolutions of Eq. (13) with the excitation pulse. Experimental data and theoretical predictions match remarkably well, further showing the possibility to retrieve transport parameters in cylindrically-shaped diffusive materials.

As a last step, we note that the tails of the time-resolved profiles are described by a single exponential decay with a decay rate Γ, which is the lowest eigenvalue of the diffusion equation in the presence of absorption in Eq. (13), i.e.,

$$\Gamma = D(\frac{\alpha_1^2}{R_e^2} + \frac{\pi^2}{L_e^2} + \frac{3}{\ell_t \ell_a}). \tag{15}$$

A plot of the measured decay rates, Γ, for all sample thicknesses L considered in this study at a wavelength of 515 nm is shown in Fig. 3(d) (red stars). Fits of Eq. (15) to the data yield $\ell_t = 48 \pm$

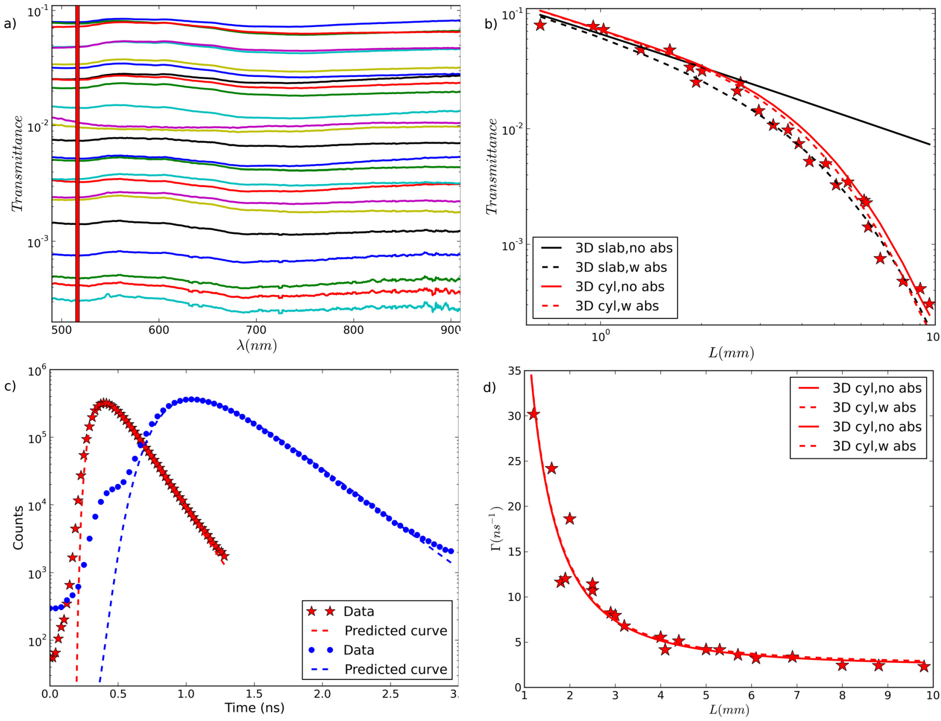

Fig. 3. (a) White light all-angle integrated transmittance of the SiO_2(HIPE) monoliths for 25 thicknesses (from top to bottom: the shortest to the longest) as a function of wavelength. The intersections of these plots with the vertical line drawn at $\lambda = 515$ nm provide the transmittance as a function of thickness (red stars) at this wavelength (b). The black solid (dashed) line shows the best fit of $T(L)$ performed by the standard diffusion equation, without (with) absorption, while the red dashed and solid lines show the best fit of $T(L)$ by Eq. (14) (including absorption) and the curve when absorption is neglected, respectively. (c) Time of flight experiments performed on 3.2 mm(red stars) and 6.9 mm (blue circles) thick samples. The corresponding dashed lines show the predicted trends of $T(L,t)$ by Eq. (13), according to the values $\ell_t = 48$ μm and $\ell_a = 0.954$ m determined in (b). (d) Exponential decay rates of the tail of $T(L,t)$ versus L (red stars). The red dashed and solid lines show the best fit of $T(L)$ by Eq. (15) (including absorption) and the curve when absorption is neglected, respectively.

3 μm and $\ell_a = 1.2 \pm 3.7$ m, which are in very good agreement with the values obtained from the steady-state measurements (Fig. 3(b)). Again, a comparison with the curve expected for $\ell_t = 48\,\mu$m and no absorption highlights the negligible role of material absorption, explaining also the very large uncertainty on ℓ_a. This therefore confirms the validity of our transport parameter recovery and of our interpretation of the results.

5. Conclusion

In conclusion, we have investigated, both theoretically and experimentally, the diffusion of light in cylindrically-shaped disordered materials, whose diameter was comparable to their thickness. We have manufactured SiO_2(HIPE) monoliths exhibiting a broad pore-size distribution centered around 19 μm. These systems resemble certain biological tissues and thus, could be

#206709 - $15.00 USD Received 18 Feb 2014; accepted 7 Mar 2014; published 24 Mar 2014

used as testbeds for optical spectroscopy techniques. We have developed a model of diffusion in finite cylinders to obtain analytical expressions for the steady-state and time-resolved transmission along the cylinder axis. These expressions have been validated by a comparison with Monte Carlo random walk simulations. Steady-state and time-resolved measurements have been performed on samples with varying thickness and the transport mean free path and material absorption length have been retrieved from fits of the experimental curves with the derived analytical expressions. Our results unambiguously show that the scattering losses on the lateral sides of the cylinder behave in a similar way as material absorption losses. Thus, neglecting the finite lateral sample size in the retrieval of the photon transport parameters can lead to a significant error in the estimation of the material absorption length. On the other hand, the problem is completely resolved when the analytical expressions for diffusion in finite cylinders are used. The recognition of this geometrical effect may be important in several practical cases, including biological tissue samples, pharmaceutical tablets, and macroporous solar cell photoanodes.